Turkish Journal of Electrical Engineering & Computer Sciences

http://journals.tubitak.gov.tr/elektrik/

Research Article

Turk J Elec Eng & Comp Sci
(2016) 24: 656 – 668

doi:10.3906/elk-1310-28

Design and analysis of a novel UWB bandpass filter using 3-D EM simulation-based neural network model with HSA

Salih DEMİREL*, **Cafer UYANIK**
Department of Electronics and Communication Engineering, Yıldız Technical University, İstanbul, Turkey

Received: 03.10.2013 • **Accepted/Published Online:** 03.01.2014 • **Final Version:** 05.02.2016

Abstract: This paper presents a new systematic analysis and design of the ultrawide-band bandpass filter by using the 3-D electromagnetic simulation-based multilayer perceptron neural network (MLP NN) model of unit elements. This MLP NN model is utilized efficiently as a fast and accurate model within a harmony search algorithm (HSA) procedure to determine the resultant optimum microstrip structure geometry. Moreover, the validity and efficiency of the HSA is manifested by comparing it with those of the standard metaheuristics, which are genetic and particle swarm algorithms. The filter that shows the best performance is designed and realized. Measurements taken from the realized filter demonstrate the success of this approximation over the band range of 3.1 GHz to 10.6 GHz, with a flat group delay performance within that range.

Key words: Harmony search algorithm, ultrawide-band bandpass filter, multilayer perceptron neural network

1. Introduction

The 3.1–10.6 GHz unlicensed ultrawide-band (UWB) [1] frequency bandwidth, dedicated by the Federal Communications Commission in February 2002, holds an important place for applications of microwave and wireless communication systems. Since the day of its dedication this frequency bandwidth has been one of the most popular study fields among researchers in radiofrequency (RF) technology. The broadband feature is particularly attractive for applications in high data-rate communication systems. One of the most important components in communication systems that operate at UWB frequencies is the bandpass filter (BPF).

Designing a BPF of high quality, wide bandwidth, compact size, low insertion loss, and wideband rejection is still a challenging task in the design of receivers and transmitters in a RF/microwave communication system. These components are usually built into a microstrip or coplanar waveguide technology for cost reduction and easy integration purposes. The microstrip BPF has been studied and improved as an important building block in the design of microwave circuits and systems that permit signals to pass in the desired range of frequencies and reject all other frequencies [2]. The UWB BPF has been designed and presented with different evolution algorithms [3,4] and methods that are subject to its features (e.g., notches, harmonic suppression) [5–8] and structures (e.g., defected ground structure, right/left-hand material) [9–18].

Contemporary UWB BPF design is a challenging task that requires the optimization of dimensional parameters. In most cases the analytical models are not available; therefore, electromagnetic (EM) simulation and simulation-driven optimization are ubiquitous in modern filter design. Employment of EM solvers directly

*Correspondence: salihd@yildiz.edu.tr

in the optimization loop may be impractical because of intensive CPU usage. Therefore, fast and accurate models are desperately needed for the efficient design and analysis of the filter.

In the current study, a new design topology that is efficient and fast for the design of the UWB BPF is presented. This design topology can easily be applied to all other strip lines. One of the original aspects of our research is that this design can be applied to all kinds of desired geometrical shapes and efficient results can be obtained. Our design basically includes 3 unit elements, shunt stubs (SSs), radial stubs (RSs), and the defected ground structure (DGS), connected in a cascade structure. Since a 3-D EM simulator is very inefficient for an optimization procedure, novel, accurate, and rapid software techniques must be employed in the design optimization of the filters. The artificial neural network (ANN) and the harmony search algorithm (HSA) are suggested for the analysis and design of the bandpass filter. The HSA has been applied for different kinds of optimization problems [19–24]. Comparisons of the HSA with other evolutionary algorithms like the genetic algorithm (GA), particle swarm optimization (PSO), etc. can be found in [25,26]. In the current research, a database was formed with a 3-D EM simulator for each unit element; it was used to train the multilayer perceptron (MLP) ANN model. Therefore, highly accurate and fast MLP network models of the unit elements were created. These models were used to design the UWB BPF cooperating with an actual, efficient HSA. The performance of the HSA was compared with those of the standard metaheuristics, GA and PSO.

The organization of the paper is as follows: the next section focuses on the unit element design analysis, where first the analysis stage of S parameters' behavior of the element is introduced using the MLP NN technique; in the third part, the HSA process is given to optimize the defined objective function using the MLP NN model; the design procedure and comparisons of the BPF are presented in Section 4; and the conclusion is presented in Section 5.

2. Unit elements design analysis

2.1. Unit elements

In this study, 3 suitable unit elements for filter topology are used. These are: 1) SSs [2], 2) RSs [27], and 3) the DGS [9–11]. The characterizations of these unit elements are managed by changing their geometrical shapes within determined limits with respect to the design goal. These limits are chosen depending on the compact structure and frequency response of the filter. The SSs behave like high-pass filters, the RSs show properties of band-stop filters, and the (DGS) operates either as a low-pass or band-stop filter, as seen in Figures 1–3 with their geometrical shape and equivalent circuits, respectively.

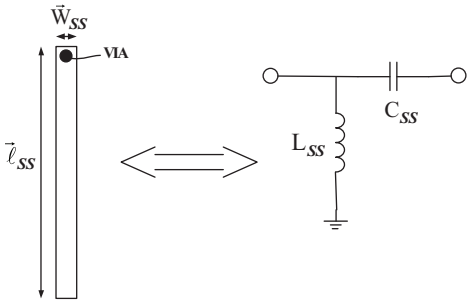

Figure 1. A shunt stub unit element and the equivalent circuit.

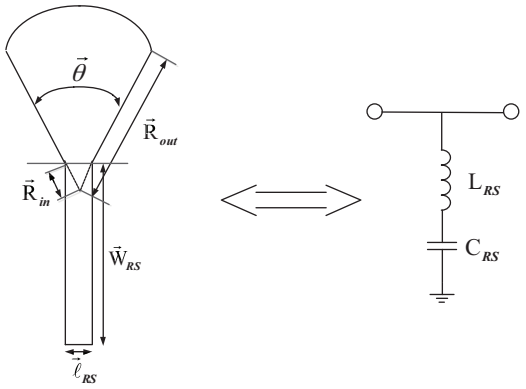

Figure 2. A radial stub unit element and the equivalent circuit.

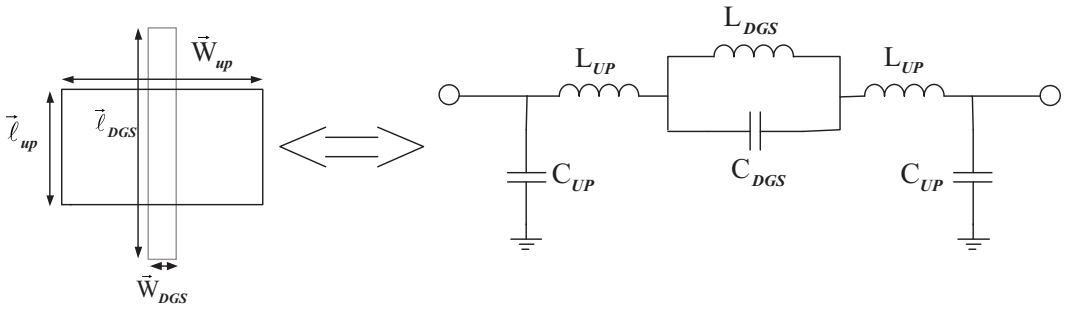

Figure 3. A defected ground structure with a microstripline unit element and the equivalent circuit.

2.2. The MLP ANN model

In this work, one of the most common neural network architectures, the MLP, is used [28–31]. A MLP network consists of two types of layers: hidden and output. Hidden layers are the layers that have the weighting coefficient matrix, the summation and multiplication operators, the bias vector b, the transfer function boxes, and the output vectors. The layer that is generated by the network output is called an output layer.

During the training process of the ANN, an increase of the iteration number will cause a decrease of the rms errors of both the training and validation. The ith output for the Pth training pattern can be described as:

$$Y_p(i) = \sum_{k=1}^{N+1} W_{oi}(i,k)X_P(k) + \sum_{j=1}^{N_h} W_{oi}(i,j)O_P(j). \tag{1}$$

In Eq. (1), $W_{oi}(i,\ k)$ represents the weight from the input nodes to the output nodes, and $W_{oi}(i,\ j)$ represents the weight from ith the hidden node to the jth output node. X_P corresponds to the N-dimensional input vector, Y_P corresponds to the M-dimensional output vector, and O_P corresponds to the activation for the trained network for the Pth pattern. The performance criteria of the network are measured by the mean square error (MSE), expressed by:

$$MSE = \frac{1}{N}\sum_{p=1}^{N_v} E_p = \frac{1}{N}\sum_{p=1}^{N_v}\sum_{i=1}^{M} \left(t_p(i) - y_p(i)\right)^2, \tag{2}$$

where:

$$E_p = \sum_{i=0}^{M} \left[t_p(i) - y_p(i)\right]^2. \tag{3}$$

In Eq. (2), E_p corresponds to the error for the Pth pattern, N_v refers to the training dataset, t_p is the requested output, and y_p corresponds to the M-dimensional output vector from the trained network for the Pth pattern.

In our design procedure, first a black-box analysis model (Figures 4–6) was composed for the unit elements. In the MLP NN analysis model, the 3-dimensional SS, 5-dimensional DGS, and 5-dimensional RS are mapped into the 4-dimensional S parameter space in their own model. The 3-dimensional SS space consists of input variables of $\vec{W}_{SS}, \vec{\ell}_{SS}, f$, which refer to microstrip width, length, and frequency in Figure 4, respectively. The 5-dimensional DGS space consists of input variables of $\vec{W}_{DGS}, \vec{\ell}_{DGS}, \vec{W}_{up}, \vec{\ell}_{up}, f$, which refer to the width of the DGS, length of the DGS, upper-side microstrip width, length, and frequency in Figure 5, respectively. The 5-dimensional RS space consists of input variables of $\vec{W}_{RS}, \vec{\ell}_{RS}, \vec{R}_{out}, \vec{\theta}, f$, which refer to microstrip width, length, outer radius of the stub, angle of the stub, and frequency in Figure 6, respectively. The inner radius R_{in} can easily be obtained from the known microstrip width W:

$$R_{in} = \frac{W}{2.\sin(\theta/2)}. \tag{4}$$

Hence, the S parameter spaces, which are of $|S_{11}|, \angle S_{11}, |S_{21}|, \angle S_{21}$ magnitude, and the angles of S_{11}, S_{21} of the unit elements are defined as the output of this analysis model.

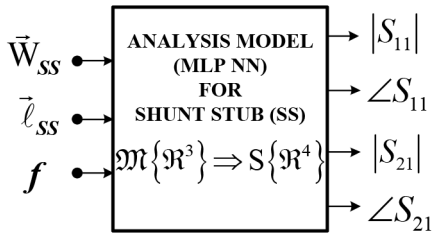

Figure 4. A black-box model of the SS unit cell with the MLP ANN model.

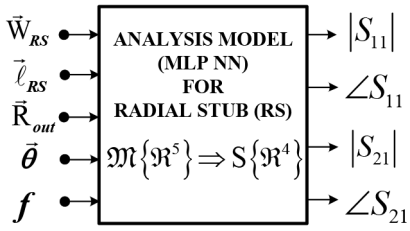

Figure 5. A black-box model of the RS unit cell with the MLP ANN model.

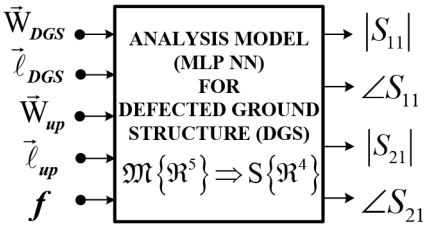

Figure 6. A black-box model of the DGS unit cell with the MLP ANN model.

The structure of our ANN model consists of an input layer, two hidden layers, and an output layer. The hyperbolic tangent function is applied as the activation function for all the hidden neurons. The Levenberg–Marquardt algorithm is applied in the optimization of the network parameters. The structure of the ANN model for the unit elements consists of 3 and 5 input neurons, 4 output neurons, and 2 hidden layers, each with 10 neurons. The network training output dataset corresponds with the input dataset, which consists of dimension ranges of elements, as seen in Table 1. It is generated using the 3-D Computer Simulation Technology Microwave Studio (CST MWS). The total training data numbers of the neural network for each frequency of

SS, RS, and DGS are 154, 400, and 3.168, respectively. Estimated results of the MLP ANN and CST MWS results for the SS element are compared in Figures 7a and 7b. According to the results, the accuracy of the model is 99.3% and the model is approximately 240 times faster than a 3-D simulator for 2.2 GHz CPU and 8 GB memory.

Table 1. Dimension ranges of unit elements for training data.

Unit elements	Input variables	Min. value	Max. value	Interval	Data number
SS	W_{SS} (mm)	0.4	3	0.2	14
	ℓ_{SS} (mm)	5	6	0.1	11
	f (GHz)	0.2	20.2	1	21
RS	W_{RS} (mm)	0.5	2	0.5	4
	ℓ_{RS} (mm)	0.2	1	0.2	5
	R_{out} (mm)	0.4	2	0.4	5
	θ ($^\circ$)	45	90	15	4
	f (GHz)	0.2	20.2	1	21
DGS	W_{DGS} (mm)	0.5	1	0.1	3
	ℓ_{DGS} (mm)	4	6	0.4	6
	W_{up} (mm)	2	4	0.2	11
	ℓ_{up} (mm)	3	6	0.2	16
	f (GHz)	0.2	20.2	1	21

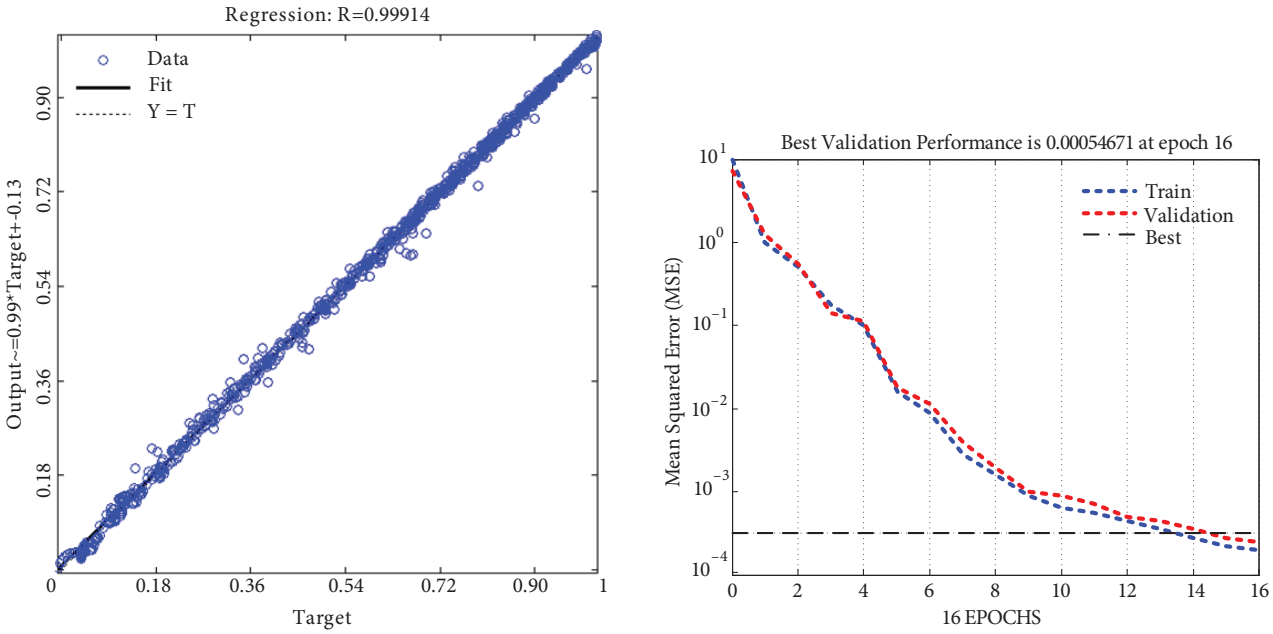

Figure 7. (a)A linear regression scatter plot for the SS element model training MSE error = 3.2912×10^{-4}. (b) Mean squared error variations of the MLP NN model of the SS element.

3. The optimization process

3.1. The harmony search algorithm

The HSA is an optimization instrument that is employed to optimize multiobjective functions to achieve the best harmony among variables. It performs like an orchestra conductor that facilitates the different instruments

to play in harmony. The obtained best harmony assists us to find the global minimum of optimization problems. In an optimization problem, each variable is represented by a player. Players play their instruments within a possible range that is subject to the type of musical instrument. All of the music that is performed by all of the players at one time produces a solution vector. The best solution vectors are selected by the algorithm and the worse ones are removed until the listeners are satisfied [32].

The HSA consists of 4 terms: harmony memory (HM), harmony memory size (HMS), harmony memory considering rate (HMCR), and pitch adjusting range (PAR). The HM matrix of Eq. (5) includes arbitrarily produced solution vectors that rank subjects to the values of the objective function, f(x) [32].

$$HM = \begin{bmatrix} x^1 & x^2 & x^3 & \dots & HMS \end{bmatrix}^T \tag{5}$$

HMCR and PAR are used to enhance the solution vector. HMCR, which has a range of 0 to 1, is defined as the probability rate of picking a variable from previous values in the HM. For example, if the HMCR is 0.9, there is a 90% probability that the design variable values will be selected from the previously stored values in the HM matrix and a 10% probability that they will be selected from the entire possible range. It is not desirable for the HMCR value to be 1 because the solution may not be within the stored HM. The PAR parameter is implemented to arrange the rate of adjustment for the pitch chosen from the HM and its value changes between 0 and 1. In that case, if a PAR parameter is 0.2, the algorithm will choose a neighboring value with 20% HMCR probability. The pitch adjustment for x_1 is applied as

$$x_1 \leftarrow x_1 + \alpha, \tag{6}$$

where α is the value of bw $\times$ u(–1,1), bw is a random distance bandwidth for the continuous design variable, and u(–1, 1) uniformly distributes between –1 and 1 [32]. It is investigated to decide whether it should be pitch-adjusted using the PAR parameter for every component of the new harmony vector. The HMCR, PAR, and HMS (which is the length of the HM) parameters are determined by the user.

$$0 < HMCR < 1 \tag{7}$$

$$0 < PAR < 1 \tag{8}$$

Figure 8 represents the optimization procedure of the HSA, which consists of 5 main steps, as follows:

Step 1. Launch the optimization problem and define optimization parameters.

Step 2. Launch the HM matrix.

Step 3. Improvise a new harmony from the HM.

Step 4. Update the HM.

Step 5. Iterate Steps 3 and 4 until the termination criteria are met [32].

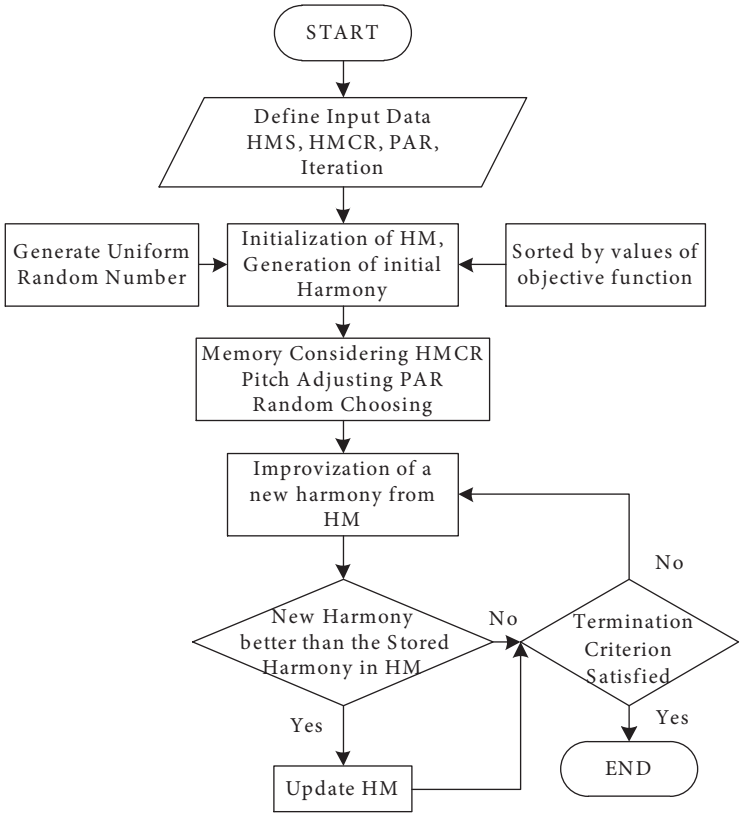

Figure 8. A flowchart of the harmony search algorithm.

The HSA tries to find a solution vector using the defined variable within the range of the HM. If the obtained solution vector is better than the worst one in the HM, the new vector will be added to the HM and the old one will be expelled. This procedure repeats until certain termination criteria are satisfied [32].

3.2. Cascaded microstrip structures

Microwave circuits that can be represented as cascaded connections of two-ports can be analyzed very effectively with ABCD matrices [33]. For the case of n two-ports in a cascade, the resultant matrix is given by Eq. (9).

$$\begin{bmatrix} A & B \\ C & D \end{bmatrix} = \begin{bmatrix} A_1 & B_1 \\ C_1 & D_1 \end{bmatrix} \begin{bmatrix} A_2 & B_2 \\ C_2 & D_2 \end{bmatrix} \cdots\cdots\cdots \begin{bmatrix} A_n & B_n \\ C_n & D_n \end{bmatrix} \tag{9}$$

According to this, the whole filter structure could be analyzed as cascade-connected main unit elements. First the ABCD parameters of each element are calculated separately and then they are combined by using Eq. (9). In our design we use 5 SSs, 2 microstrip lines, 4 RSs, and 6 DGSs. Thus, the ABCD matrix number n is 17 and it is as follows in Eqs. (10) and (11):

$$[T]^n = \begin{bmatrix} A_n & B_n \\ C_n & D_n \end{bmatrix}, \tag{10}$$

$$\begin{bmatrix} A & B \\ C & D \end{bmatrix}_{BPF} = [T]^1_{SS_1} [T]^2_{ML_1} [T]^3_{RS_1} [T]^4_{DGS_1} \ldots [T]^{17}_{SS_5}, \tag{11}$$

where the relations describing the transformation between the S and T(ABCD) matrices follow in Eqs. (12)–(15) [33]:

$$A = \frac{Z_{N1}^{*} + Z_{N1}S_{11} - Z_{N1}^{*}S_{22} - Z_{N1}\Delta_S}{2S_{21}\sqrt{Re\{Z_{N1}\}\,Re\{Z_{N2}\}}}, \tag{12}$$

$$B = \frac{Z_{N1}^{*}Z_{N2}^{*} + Z_{N1}Z_{N2}^{*}S_{11} + Z_{N1}^{*}Z_{N2}S_{22} + Z_{N1}Z_{N2}\Delta_S}{2S_{21}\sqrt{Re\{Z_{N1}\}\,Re\{Z_{N2}\}}}, \tag{13}$$

$$C = \frac{1 - S_{11} - S_{22} + \Delta_S}{2S_{21}\sqrt{Re\{Z_{N1}\}\,Re\{Z_{N2}\}}}, \tag{14}$$

$$D = \frac{Z_{N2}^{*} - Z_{N2}^{*}S_{11} + Z_{N2}S_{22} - Z_{N2}\Delta_S}{2S_{21}\sqrt{Re\{Z_{N1}\}\,Re\{Z_{N2}\}}}. \tag{15}$$

The inverse relations are:

$$S_{11} = \frac{AZ_{N2} + B - CZ_{N1}^{*}Z_{N2} - DZ_{N1}^{*}}{AZ_{N2} + B + CZ_{N1}Z_{N2} + DZ_{N1}}, \tag{16}$$

$$S_{21} = \frac{2\sqrt{Re\{Z_{N1}\}\,Re\{Z_{N2}\}}}{AZ_{N2} + B + CZ_{N1}Z_{N2} + DZ_{N1}}, \tag{17}$$

where $Z_{N1} = 50\Omega$ and $Z_{N2} = 50\Omega$ are the reference impedances of two-port ports and $\Delta_S = S_{11}S_{22} - S_{12}S_{21}$.

In the calculation of the ABCD parameters, the S parameters of each element could be obtained with their ANN model. Following the computation of the ABCD matrix, the S parameters of the filter are computed using the inverse relations of Eqs. (16) and (17). Furthermore, there is no need to investigate S_{12} and S_{22} of the filter because it is known that employed unit elements are reciprocal, which means $S_{11} = S_{22}$ and $S_{12} = S_{21}$ [33].

3.3. Objective function

During the optimization process, the most suitable dimensions are searched to provide the desired UWB filter response. In order to achieve these, the necessary objective function is described as follows in Eq. (18).

$$Objective = W_1.\in_1 + W_2.\in_2 + W_3.\in_3 \tag{18}$$

$$\in_1 = (1 - |S_{11}| + |S_{21}|)|_{\Delta f_1} \tag{19}$$

$$\in_2 = (1 + |S_{11}| - |S_{21}|)|_{\Delta f_2} \tag{20}$$

$$\in_3 = (1 - |S_{11}| + |S_{21}|)|_{\Delta f_3} \tag{21}$$

Here, $\Delta f_1 = 0.2 - 3.1GHz, \Delta f_2 = 3.1 - 10.6GHz$, and $\Delta f_3 = 10.6 - 20GHz$. The weighting coefficients W_1, W_2, W_3 are 1/3, 1, and 1/4, respectively. Moreover, the optimization parameters HMS, HMCR, and PAR are adjusted as 25, 0.8, and 0.4, respectively. The optimization process is completed as soon as the iteration number reaches its maximum value or the predefined cost value.

4. Design and comparison of the UWB bandpass filter

In this section, the design procedure of the filter is explained. First the characteristics of the unit elements (SS, RS, and DGS) are analyzed separately. According to these, the SS behaves as a high-pass filter, the RS has a band-stop filter characteristic operating at a narrow band, and the DGS could be either a band-pass or a band-stop structure. In this study, the DGS is chosen as a band-stop filter and is used for harmonic rejection at the second and third harmonic frequencies of the filter. In the design, these elements are connected to each other in a cascade and the dimensions are adjusted by HSA optimization to obtain the requested return loss, transition, and harmonic rejection subject to the objective function. Instead of a 3-D EM simulation model for each element, the highly accurate MLP ANN model is used to expedite the optimization process. The general design procedure is given in Figure 9. Filter selectivity is provided by the order of the filter.

RO-4350, which has dielectric permittivity $\varepsilon_r = 3.48$, substrate thickness h = 1.52 mm, copper thickness t = 35 μm, and tangent loss $\tan\delta = 0.002$, is used as a substrate for the unit elements. SMA connectors are utilized at the input-output ports. According to the optimization results, the obtained UWB BPF operates between 3.1 GHz and 10.6 GHz. After the optimization process, the designed filter is fabricated and measured. An illustration and a picture of the filter are shown in Figures 10 and 11, respectively. Moreover, the outer dimension of the manufactured filter is 7.5 $\times$ 2 cm^2. Detailed dimensions are given for the SSs, RSs, DGSs, and microstrip lines in Table 2.

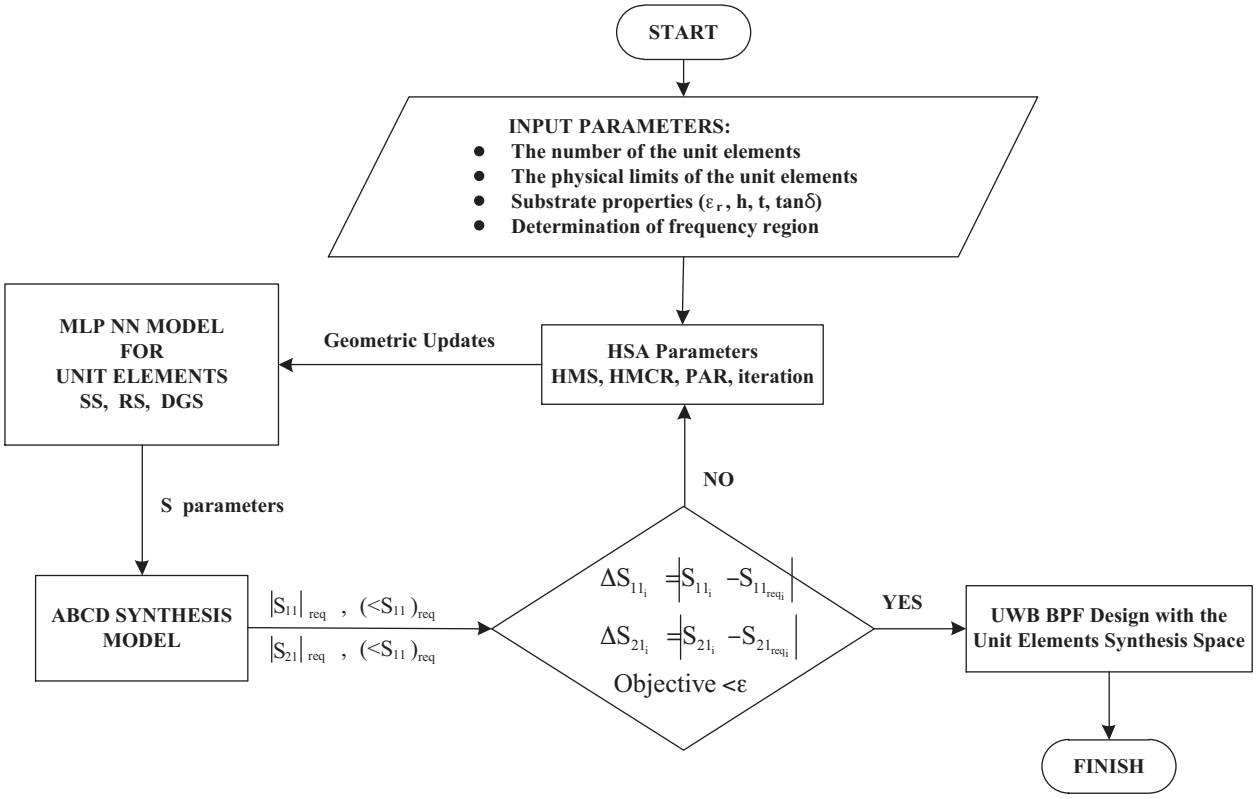

Figure 9. A general design procedure for a UWB bandpass filter.

Measurement results and CST MWS results are compared, as seen in Figure 12. According to these results, the insertion loss of the filter is above –2 dB at the pass-band and there is little insertion loss at high frequencies because of the connectors. The return loss of the filter is below –10 dB at the pass-band. The

rejection band of the filter reaches 25 GHz and the second and third harmonic suppressions of the filter are greater than 20 dB. The sharpness of the filter is also good at low and high frequencies. The measured group delay of the filter is flat all over the operation band, as given in Figure 13.

Table 2. Solutions of the unit elements.

Unit elements	Input variables	1st element	2nd element	3rd element	4th element	5th element	6th element
SS	W_{SS} (mm)	1.6	2	3	2.2	0.4	-
	ℓ_{SS} (mm)	5.6	5.2	5.4	5.4	5.6	-
RS	W_{RS} (mm)	0.5	0.5	0.5	0.5	-	-
	ℓ_{RS} (mm)	0.2	0.2	0.2	0.2	-	-
	R_{out} (mm)	0.8	1.2	1.2	0.8	-	-
	θ (°)	60	45	45	60	-	-
DGS	W_{DGS} (mm)	0.6	0.6	0.6	0.6	0.6	0.6
	ℓ_{DGS} (mm)	6	5.6	5.2	5.2	5.6	6
	W_{up} (mm)	3.8	3.2	3	2.8	2.8	3
	ℓ_{up} (mm)	6	4.2	5	3.8	4.6	3.6
ML	W_{SS} (mm)	4	3.2	-	-	-	-
	ℓ_{SS} (mm)	4.8	5	-	-	-	-

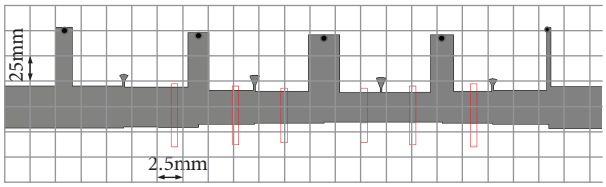

Figure 10. A scalable filter drawing with a grid background.

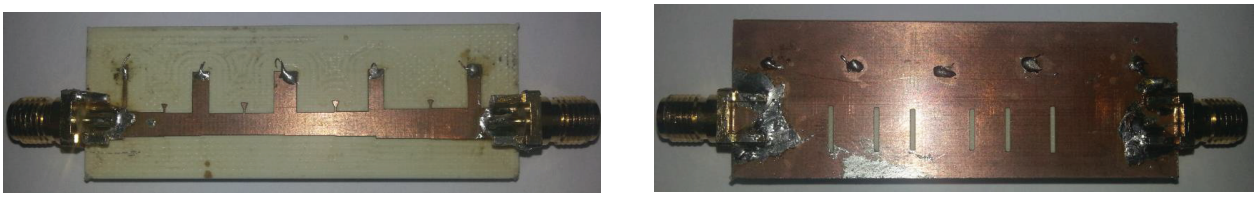

(a) (b)

Figure 11. Photographs of the fabricated UWB BPF: (a) top layer; (b) bottom layer.

Since the soldering process was not ideal, as seen in Figure 11, some degradation in the frequency response was observed, especially at higher frequencies (Figure 12). The $|S_{21}|$ degradation seems to be 1 to 2 dB due to minor impedance changes caused by bulk soldering at some locations. The transition from a coax environment to a microstrip medium actually needs a better process for a good impedance match. On the other hand, bulk soldering at the ends of the stubs may shift the resonance frequencies down, as it effectively increases the electrical length. At the high frequency edge of the band, the imperfect soldering degrades the selectivity as well. However, these effects appear minor and acceptable in $|S_{21}|$ and $|S_{11}|$ responses.

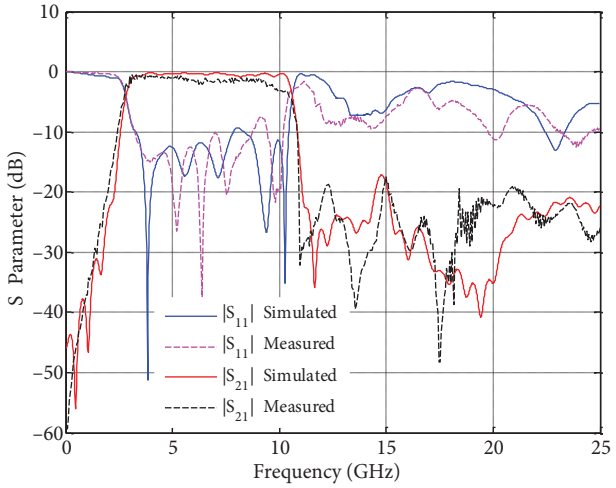

Figure 12. Simulated and measured S parameters of the designed UWB BPF.

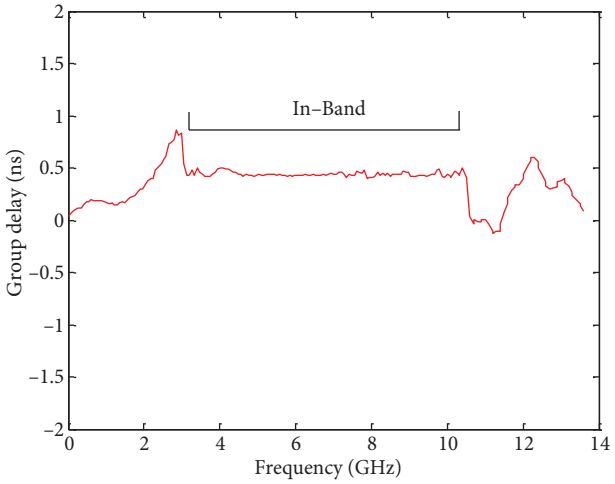

Figure 13. Measured group delay of the designed UWB BPF.

The Intel Core i7 CPU, 2.20 GHz Processor, 8 GB RAM is used for the optimization. It should be noted that all variations for the proposed UWB filter result from the first time run of the algorithms for a maximum iteration number of 70, with the user parameters chosen compatible, as shown in Table 3. Moreover, in Table 4 the cost results of 10 time tries and 70 iterations of the HSA and other standard metaheuristic algorithms for the same filter are shown. In the worked examples, the cost value reached at 65 iterations is used, which is equal to 0.3764; that is smaller than the cost values of the GA and PSO. The corresponding execution times for the HSA, GA, and PSO were 61, 79, and 66 s, respectively (Table 5). Finally, one can infer that the HSA algorithm is preferable as compared with these counterparts.

Table 3. A comparison among the resulting algorithms.

Algorithm	Population	Maximum iteration	Special parameters
HSA	25	70	HMCR = 0.8, PAR = 0.4
GA	25	70	Gaussian mutation
PSO	25	70	Learning factors $c_1 = c_2 = 2$

Table 4. Cost results of 10 time tries and 70 iterations of the standard metaheuristic algorithms and HSA.

Algorithm	Worst (max)	Best (min)	Average (mean)
HSA	1.641	0.376	0.511
GA	3.01	0.444	0.819
PSO	1.221	0.523	0.808

Table 5. Benchmarking at the 65th iteration for the best try.

Algorithm	Cost	Execution time (s)
HSA	0.3764	61
GA	0.444	79
PSO	0.523	66

5. Conclusion

In the current work, an accurate and fast MLP NN model based on the EM simulator is introduced to be employed in both the design and analysis of the UWB BPF. All the building stages of the MLP NN model and its utilization in the design and analysis of a UWB BPF are given in detail as a general systematic method that can be applied to different types of filters. The unit elements' MLP NN models are built to be used in an original, simple, and efficient metaheuristic novel optimization algorithm. The accuracy of the HSA method is verified by comparing the results with their analytical counterparts. The method is compared with those of the competitive population-based algorithms and the method's fast convergence feature is verified. It is shown that this approach can also be applied as a robust method for the design and analysis of filters built by arbitrarily shaped geometries. Therefore, the proposed method can be considered as a significant contribution to novel software technology. After the optimization process, the designed UWB BPF was fabricated and measured. The measured results showed good agreement with the simulation.

Acknowledgment

The authors would like to thank the Turkish Air Force Academy for its support of the current work.

References

[1] Federal Communications Commission. Revision of Part 15 of the Commission's rules regarding ultra wideband transmission system first report and order. Tech Rep ET Docket 2002; 48: 98–153.

[2] Matthaei GL, Young L, Jones EMT. Microwave Filters, Impedance-Matching Networks, and Coupling Structures. Norwood, MA, USA: Artech House, 1980.

[3] Coudos SK, Zaharis ZD, Yioultsis TV. Application of a differential evolution algorithm with strategy adaptation to the design of multi-band microwave filters for wireless communications. Prog Electromagn Res 2010; 109: 123–137.

[4] Wu B, Li B, Su T, Liang CH. Equivalent-circuit analysis and lowpass filter design of split-ring resonator DGS. J Electromagnet Wave 2006; 20: 1943–1953.

[5] Zhu YZ, Xie YJ. Novel microstrip bandpass filters with transmission zeros. Prog Electromagn Res 2007; 77: 29–41.

[6] Park J, Kim JP, Nam S. Design of a novel harmonic-suppressed microstrip low-pass filter. IEEE Microw Wirel Co 2007; 17: 424–426.

[7] Shaman H, Hong JS. A novel ultra-wideband (UWB) bandpass filter (BPF) with pairs of transmission zeroes. IEEE Microw Wirel Co 2007; 17: 121–123.

[8] Deng HW, Zhao YJ, Zhang XS, Zhang L, Gao SP. Compact quintuple-mode UWB bandpass filter with good out-of-band rejection. Prog Electromagn Res Lett 2010; 14: 111–117.

[9] Oskouei HD, Forooraghi K, Hakkak M. Guided and leaky wave characteristics of periodic defected ground structures. Prog Electromagn Res 2007; 73: 15–27.

[10] Ahn D, Park JS, Kim CS, Kim J, Qian Y, Itoh T. A design of the low-pass filter using the novel microstrip defected ground structure. IEEE T Microw Theory 2001; 49: 86–93.

[11] Lee JK, Kim YS. Ultra-wideband bandpass filter with improved upper stopband performance using defected ground structure. IEEE Microw Wirel Co 2010; 20: 316–318.

[12] Li R, Zhu L. Compact UWB bandpass filters using stub-loaded multiple-mode resonator. IEEE Microw Wirel Co 2007; 17: 40–42.

[13] Huang JQ, Chu QX. Compact UWB band-pass filter utilizing modified composite right/left-handed structure with cross coupling. Prog Electromagn Res 2010; 107: 179–186.

[14] Chou TC, Tsai MH, Chen CY. A low insertion loss and high selectivity UWB bandpass filter using composite right/left-handed material. Prog Electromagn Res C 2010; 17: 163–172.

[15] Wang JK, Zhao YJ, Qiang L, Sun Q. A miniaturized UWB BPF based on novel SCRLH transmission line structure. Prog Electromagn Res Lett 2010; 19: 67–73.

[16] Naghshvarian JM, Tayarani M. Miniature planar UWB bandpass filters with circular slots in ground. Prog Electromagn Res Lett 2008; 3: 87–93.

[17] Shobeyri M, Vadjed-Samiei MH. Compact ultra-wideband bandpass filter with defected ground structure. Prog Electromagn Res Lett 2008; 4: 25–31.

[18] An J, Wang GM, Zeng WD, Ma LX. UWB filter using defected ground structure of Von Koch fractal shape slot. Prog Electromagn Res Lett 2009; 6: 61–66.

[19] Ghosh S, Kundu D, Suresh K, Das S, Abraham A. Design of optimal digital IIR filters by using a bandwidth adaptive harmony search algorithm. In: World Congress on Nature and Biologically Inspired Computing; 9–11 December 2009, Coimbatore, India. New York, NY, USA: IEEE. pp. 481–486.

[20] Khazali AH, Parizad A, Kalantar M. Optimal reactive/voltage control by an improved harmony search algorithm. In: 23rd Canadian Conference on Electrical and Computer Engineering; 2–5 May 2010; Calgary, Canada. New York, NY, USA: IEEE. pp. 1–6.

[21] Rao RS, Narasimham SVL, Raju MR, Rao AS. Optimal network reconfiguration of large-scale distribution system using harmony search algorithm. IEEE T Power Syst 2011; 26: 1080–1088.

[22] Dexuan Z, Haikuan L, Liqun G. A modified global harmony search algorithm for robust PID controller tuning. In: Proceedings of the 30th Chinese Control Conference; 22–24 July 2011; Yantai, China. New York, NY, USA: IEEE. pp. 2158–2163.

[23] Sirjani R, Mohamed A. Improved harmony search algorithm for optimal placement and sizing of static VAR compensators in power systems. In: First International Conference on Informatics and Computational Intelligence; 12–14 December 2011; Bandung, Indonesia. New York, NY, USA: IEEE. pp. 295–300.

[24] Boroujeni SMS, Boroujeni BK, Delafkar H, Behzadipour E, Hemmati R. Harmony search algorithm for SVC controller tuning in voltage support mode. Indian Journal of Science and Technology 2011; 4: 1155–1159.

[25] Kudikala S, Sabat SL, Udgata SK. Performance study of harmony search algorithm for analog circuit sizing. In: International Symposium on Electronic System Design; 19–21 December 2011; Kochi, India. New York, NY, USA: IEEE. pp. 12–17.

[26] Agbolosu-Amison SJ, Park B, Yun I. Comparative evaluation of heuristic optimization methods in urban arterial network optimization. In: Proceedings of the 12th International IEEE Conference on Intelligent Transportation Systems; 4–7 October 2009; St. Louis, MO, USA. New York, NY, USA: IEEE. pp. 1–6.

[27] Giannini F, Ruggieri R, Vrba J. Planar circuit analysis of microstrip radial stub. IEEE T Microw Theory 1984; 32: 1652–1655.

[28] Zhang QJ, Wang F, Devabhaktuni VK. Neural network structures for RF and microwave applications. In: IEEE Antennas and Propagations International Symposium; July 1999; Orlando, FL, USA. New York, NY, USA: IEEE. pp. 2576–2579.

[29] Wang F, Devabhaktuni VK, Xi C, Zhang QJ. Neural network structures and training algorithms for RF and microwave applications. Int J RF Microw C E 1999; 9: 216–240.

[30] Burrascano P, Fiori S, Mongiardo M. A review of artificial neural networks applications in microwave computer-aided design (invited article). Int J RF Microw C E 1999; 9: 158–174.

[31] Selleri S, Manetti S, Pelosi G. Neural network applications in microwave device design. Int J RF Microw C E 2002; 12: 90–97.

[32] Lee KS, Geem ZW. A new meta-heuristic algorithm for continuous engineering optimization: harmony search theory and practice. Comput Method Appl M 2005; 194: 3902–3933.

[33] Dobrowolski JA. Introduction to Computer Methods for Microwave Circuit Analysis and Design. Norwood, MA, USA: Artech House, 1991.